Chapter 6
Analytical Methods for Carbonation Material

Abstract Interest in the accelerated carbonation of alkaline solid wastes has sharply escalated because accelerated carbonation of alkaline solid waste is an attractive method for carbon capture and utilization, due to their potential to fix gaseous CO_2 from industry into solid precipitation. The physico-chemical properties of solid wastes can be improved by carbonation, thereby increasing the potential to be used as construction materials such as supplementary cementitious materials and/or aggregates in civil engineering. In this chapter, several advanced analytical methods for material characterization are introduced. For example, an integrated thermal analysis (i.e., modified TG-DTG interpretation) is illustrated to determine carbonation parameters in alkaline solid wastes.

6.1 Integrated Thermal Analysis

Accurate determination of the contents of $CaCO_3$ formation in the course of accelerated carbonation is crucial for assessing the potential for CO_2 capture by alkaline wastes, as well as providing scientific data for interpretation of the carbonation reaction kinetics. To determine the performance of accelerated carbonation via various types of approach and process, thermoanalytical techniques have been utilized to quantify carbonation products, such as calcium carbonate ($CaCO_3$) in solid wastes. The commonly used thermoanalytical techniques include

- Thermogravimetric (TG) analysis,
- Derivative thermogravimetric (DTG),
- Differential thermal analysis (DTA), and
- Differential scanning calorimetry (DSC).

TG analysis determines the weight of sample at different temperatures under an assigned heating programs. The weight loss can be attributed to moisture evaporation and chemical decomposition of compounds into gaseous components.

P.-C. Chiang and S.-Y. Pan, *Carbon Dioxide Mineralization and Utilization*, DOI 10.1007/978-981-10-3268-4_6

Therefore, individual compounds can be quantified because the thermal decomposition temperatures vary among compounds. On the other hand, by taking numerical derivation of the TG curve, a DTG plot can be obtained to provide information on the temperature at the maximum peak and other important peak parameters.

In DSC, a sample cell and a reference were heated equally according to a preset temperature regime. When transformation of the sample occurs, the temperature difference between the sample and the reference cell is measured. The device will increase or reduce the heat input to the sample cell to maintain a zero temperature difference between the sample and the reference cell, establishing a "null balance" [1]. The quantity of the electrical energy supplied to a sample cell is usually expressed in terms of energy per unit time (e.g., watts). Therefore, the amount of energy absorbed or released by the sample can be measured with DSC.

6.1.1 Conventional Thermogravimetric (TG) Analysis

TG analysis has been considered a rapid and accurate method for determining the content of crystalline $CaCO_3$ in samples with simple composition (highly pure) [2]. In the case of cementitious materials such as cement and fly ash [3], however, it was difficult to obtain accurate quantitative amounts of $CaCO_3$ using only TG data. This is attributed to

- The way to interpret TG curves for $CaCO_3$ decomposition in a material was varied among researchers.
- The temperature ranges of thermal decomposition of $CaCO_3$ overlap the calcareous and hydrated components in these materials (as shown in Fig. 6.1).

As shown in Fig. 6.2, two of the most commonly used methods for determining the weight loss of a material by interpreting TG plot are as follows:

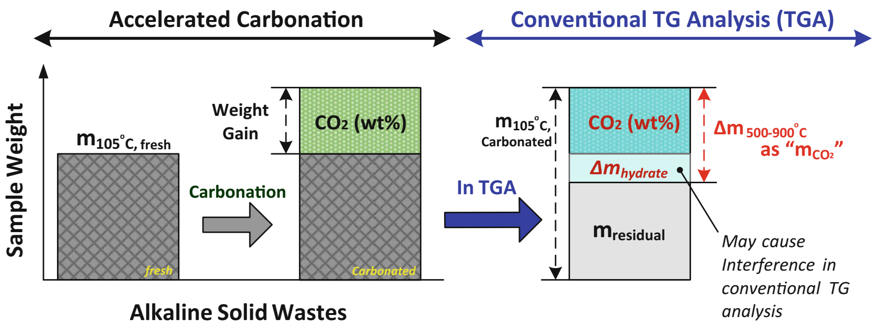

Fig. 6.1 Challenges in conventional thermogravimetric (TG) analysis for cementitious materials due to thermal decomposition of $CaCO_3$ overlap the calcareous and hydrated components. Adaptation with permission from Macmillan Publishers Ltd: ref. [24], copyright 2016

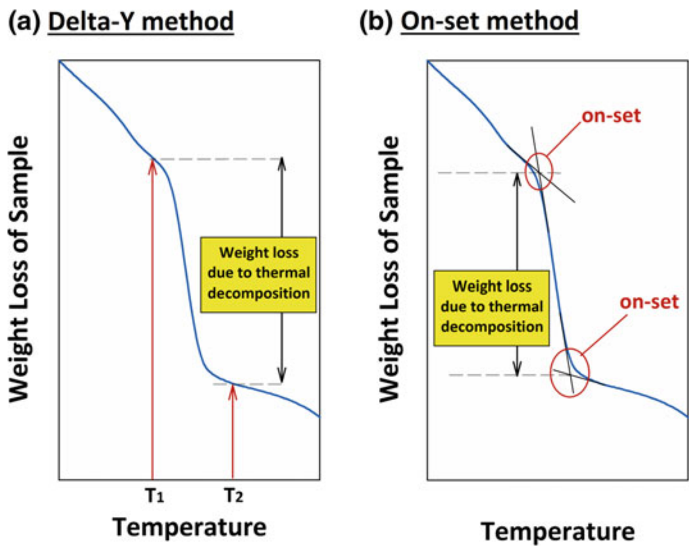

Fig. 6.2 Conventional methods on TG interpretation: **a** delta-Y and **b** on-set methods. Adaptation with permission from Macmillan Publishers Ltd: ref. [24], copyright 2016

- Delta-Y method (Fig. 6.2a): to determine the difference of sample weight directly between two specific temperatures (e.g., T_1 and T_2).
- On-set method (Fig. 6.2b): to extend the straight-line portions of the baseline and the linear portion of the upward/downward slope, mark their intersection, and determine the weight difference between these two intersections.

However, between these two conventional methods, there is a significant difference in the determined weight loss for the same TG plot. For instance, in the case of steel slag, the dehydration of calcium silicate hydrates, calcium aluminate hydrates, and other minor hydrates occurs between 105 and 1000 °C. This would result in a continuous and steady weight loss at 105–1000 °C and especially pronounce at temperatures less than 500 °C [4]. Therefore, consideration must be given to weight loss due to dehydration of the above materials when analyzing, for example, the amounts of $CaCO_3$ (weight loss typically occurs above 500 °C). Otherwise, the $CaCO_3$ contents in solid samples will be overestimated by the conventional delta-Y or on-set methods.

Table 6.1 summarizes the analytical conditions of TG, such as temperature ranges of the thermal decomposition of $Ca(OH)_2$, $MgCO_3$, and $CaCO_3$, for different solid wastes in the literature. As noted in Table 6.1, the evaluation criteria of carbonate products by TG analysis are quite different among the literature because of the wide variance in determining the temperature ranges of product decomposition. This is also largely attributed to the various ways to interpret TG plot, thereby resulting in different bases on the performance evaluation of CO_2 fixation capacity by accelerated carbonation.

Table 6.1 Analytical conditions of TG and the used decomposition temperature for $Ca(OH)_2$, $MgCO_3$, and $CaCO_3$ in different types of raw materials in the literature. Adaptation with permission from Macmillan Publishers Ltd: ref. [24], copyright 2016

Type of materials[a]	Heating rate (°C/min)	Atmosphere	Sample weight (mg)	Temperature of decomposition (°C)				Reference
				$Ca(OH)_2$	$MgCO_3$	$CaCO_3$	Carbonate	
Wollastonite	10	N_2	–	–	–	600–900	–	[5]
Serpentine	10	N_2	–	330–473	473–573	–	–	[6]
Serpentine	10	N_2			300–550			[7]
Concrete	10	–	225	430–530	–	780–900	650–950	[3]
Concrete	20	–	–	425–550	–	550–950	–	[8]
Mortar	10	Air	200	430–520		~750	–	[9]
Mortar/GBFS	10	N_2	–	>380	–	650–790	–	[10]
Steel slag	40	O_2	10–20	–	105–500	–	500–1000	[11]
Steel slag	15	N_2	~100	340–430	–	600–800	–	[12]
BOFS	10	N_2	10–20	–	–	500–780	–	[13]
BOFS	–	–	–	–	–	600–780	–	[14]
EAFS	–	Ar	–	~600	–	>600	–	[15]
CKD/sludge	–	–	–	450–550	–	700–850	–	[16]
CKD	20	N_2	~22	300–500	–	500–800	–	[17]
MSWI-BA	10	Ar	20	–	–	600–750	–	[18]
MSWI-FA	10	–	–	–	–	–	450–900	[19]
APC residue	15	Air	500	400–500	–	750–850	600–850	[20]
APC residue	10	Air	–	400–450	–	650–800	–	[21]
Cockle shell	20	N_2	10–20	–	–	700–900	–	[22]
Synthesis carbonates	50	N_2	5–10	–	515–640	620–780	–	[23]

[a]*GBFS* granulate blast furnace slag; *BOFS* basic oxygen furnace slag; *EAFS* electric arc furnace slag; *CKD* cement kiln dust; *MSWI* municipal solid waste incinerator; *FA* fly ash; *BA* bottom ash; and *APC* air pollution control

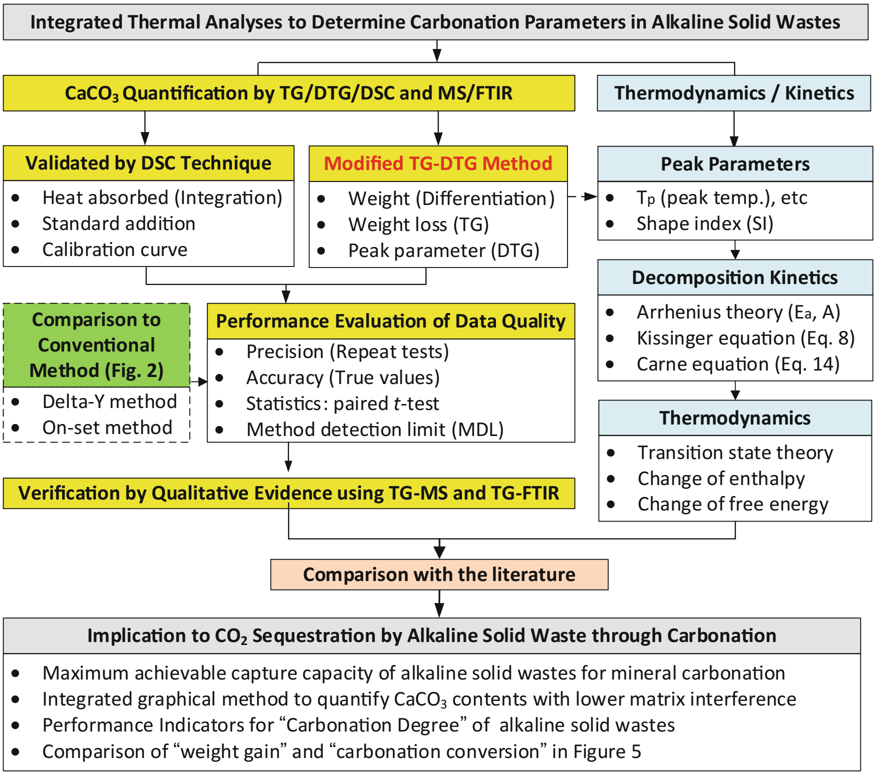

Fig. 6.3 Determination of carbonation conversion in alkaline solid wastes via integrated thermal analysis, including modified TG-DTG method and qualitative analysis via MS and FTIR

To overcome the aforementioned barriers, integrated thermal analyses (including modified TG-DTG method and qualitative analysis via MS and FTIR) are proposed as presented in Fig. 6.3. A modified TG-DTG interpretation is developed to accurately and precisely determine the carbonate content in alkaline solid wastes and validated with DSC analysis, as outlined in Sect. 6.1.2. In addition, the kinetic and thermodynamic parameters of $CaCO_3$ thermal decomposition in solid waste can be determined via various equations, as outlined in Sect. 6.1.4.

6.1.2 Modified TG-DTG Interpretation

In this section, a validated thermal analysis method (i.e., modified TG-DTG interpretation) is illustrated for accurately quantifying the $CaCO_3$ content in solid wastes. The modified TG-DTG interpretation should be generally applicable to various types of alkaline solid wastes. The standard operation procedure is provided as follows:

- Step 1: dry samples at 105 °C for at least 30 min to remove the adsorbed water before analysis,
- Step 2: place 3–10 mg of solid samples in a platinum crucible and put in TG analyzer,
- Step 3: heat sample directly from 50 to 950 °C at 10–20 °C/min under N_2 atmosphere,
- Step 4: apply the modified TG-DTG interpretation (Fig. 6.2) to determine the weight loss of certain compound, and
- Step 5: combine with other qualitative analyses (such as MS) to confirm the species of evolved gas within the temperature ranges of decomposition.

Figure 6.4 shows the modified TG-DTG interpretation for determining the $CaCO_3$ content in alkaline solid wastes. In the modified method, both the initial (T_1) and final (T_2) temperatures of $CaCO_3$ decomposition on TG plot are determined by the extrapolated on-set. The point determined by extrapolated on-set is defined as the intersection of the tangent drawn at the point of greatest slope on the leading edge of the peak with the extrapolated baseline. The weight loss due to $CaCO_3$ decomposition can then be obtained by

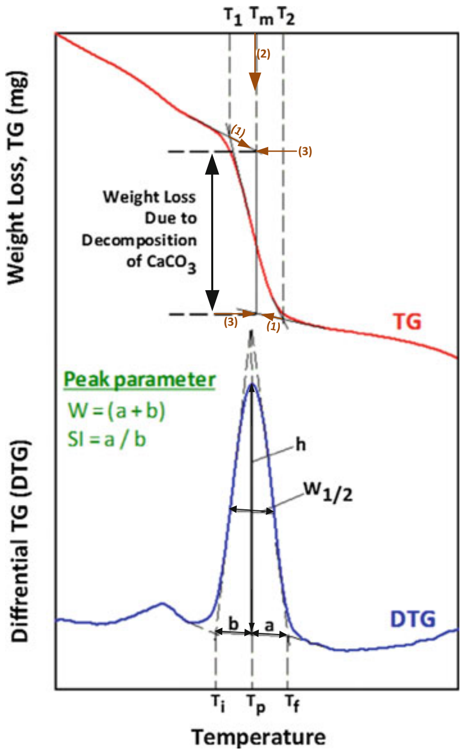

Fig. 6.4 Modified TG-DTG interpretation to determine $CaCO_3$ content in alkaline solid wastes by both TG (*upper curve*) and peak parameters from DTG (*lower curve*). Adaptation with permission from Macmillan Publishers Ltd: ref. [24], copyright 2016

- Step 1: extending the two straight-line portions of the baseline before T_1 and after T_2,
- Step 2: making a vertical line pass through the midpoint (T_m) between T_1 and T_2, and
- Step 3: determining their intersections to the baselines and vertical line. The weight loss between these two intersections was attributed to the $CaCO_3$ decomposition within the solid samples.

For the DTG curve, it can be characterized by the temperature of extrapolated on-set drawn by the beginning (T_i) and final (T_f) of the peak. The center of temperature peak (T_p), half width ($W_{1/2}$), and peak width (W) can be determined accordingly. As shown in Fig. 6.4, the shape index (SI) of the DTG peak is defined as the absolute ratio of the slope of the tangents to the DTG peak at the inflection points. Therefore, the above shape parameters of DTG can be graphically determined.

By the modified TG-DTG interpretation, a positive correlation between $CaCO_3$ content in alkaline wastes and its reactivity with CO_2 through mineral carbonation can be observed. Except for the complex and hydrated compounds in alkaline solid wastes, the weight loss versus decomposition temperature for a material can be separated into

- 50–105 °C: expulsion of surface water,
- 200–300 °C: removal of pore water,
- 400–500 °C: dehydration of crystal water (e.g., $Ca(OH)_2$),
- 500–630 °C: $MgCO_3$ decomposition, and
- 600–850 °C: $CaCO_3$ decomposition.

The matrix interference due to Ca–Al–Si hydrates presented in alkaline solid wastes can be reduced to a level of 10^{-3}. The method detection limit of the modified TG-DTG interpretation is about 0.70%, with a high precision (0.40 ± 0.25%) and accuracy (1.34 ± 0.20%) in the case of BOFS [24].

6.1.3 Key Carbonation Parameters in Solid Wastes

As shown in Fig. 6.2, the CO_2 content (denoted as "CO_2") in the sample can be determined using the modified TG-DTG method by Eq. (6.1):

$$CO_2(\text{wt\%}) = \frac{\Delta m_{CO_2}}{m_{105\,^\circ C}} \times 100 \tag{6.1}$$

where Δm_{CO_2} (mg) is the weight loss due to the decomposition of $CaCO_3$. $m_{105\,^\circ C}$ (mg) is the dry weight of the sample.

By doing so in Eq. (6.1), two key carbonation indicators can be calculated, i.e., the weight gain (%) and carbonation conversion. The weight gain (%) of the dry solid waste then can be realized using the value of CO_2 content, according to Eq. (6.2):

$$\text{Weight gain}\,(\%) = \frac{CO_2(\text{wt}\%)}{100 - CO_2(\text{wt}\%)} \times 100 \tag{6.2}$$

The carbonation conversion of solid waste (δ_{CaO}, %) can be calculated by Eq. (6.3), assuming the calcium-bearing compositions are the main reaction species:

$$\delta_{CaO} = \frac{\frac{CO_2(\%)}{100-CO_2(\%)} \times \frac{1}{MW_{CO_2}}}{Ca_{total}/MW_{Ca}} = \frac{\frac{CO_2(\%)}{100-CO_2(\%)} \times \frac{1}{MW_{CO_2}}}{CaO_{total}/MW_{CaO}} \tag{6.3}$$

where MW_{CO_2}, $MW_{Ca,}$ and MW_{CaO} are the molecular weight of CO_2 (44 g/mol), Ca (40 g/mol), and CaO (56 g/mol), respectively. Ca_{total} and CaO_{total} are the percent weight fraction of Ca (normally determined by XRF or by ICP after total digestion) and CaO (normally determined by XRF) in the fresh solid sample, respectively.

Both the weight gain (Eq. 6.2) and carbonation conversion (Eq. 6.3) determined by TGA are frequently expressed as the degree of carbonation for one target material. Figure 6.5 shows the relationship between weight gain and carbonation conversion of alkaline solid wastes. The plot of carbonation conversion versus weight gain is a straight line, and the slope of the straight line is related to the CaO

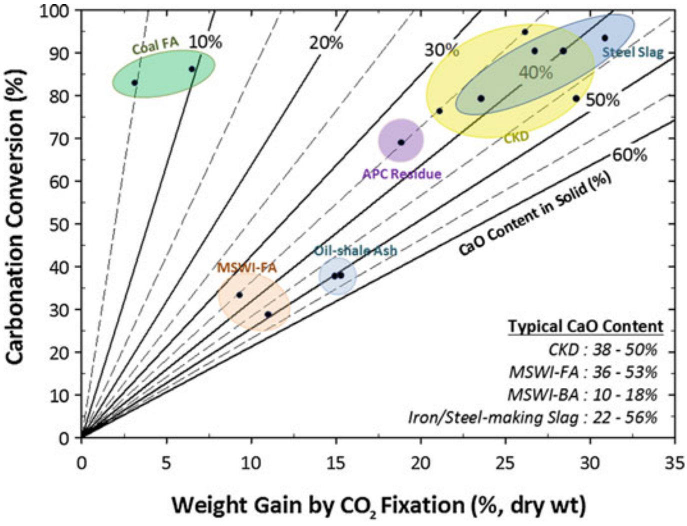

Fig. 6.5 Profile of carbonation conversion and weight gain per dry weight for different solid wastes, including cement kiln dust (CKD), municipal solid waste incinerator (MSWI), fly ash (FA), and bottom ash (BA). Adaptation with permission from Macmillan Publishers Ltd: ref. [24], copyright 2016

content in the solid. It is noted that alkaline solid wastes, such as steel slag and fly ash, have been recognized as effective materials for CO_2 sequestration by mineral carbonation. For example, the cement kiln dust (CKD) and steel slag exhibit the relatively higher CaO content (i.e., 30–50%) and CO_2 capture capacity by the maximum achievable conversion technologies as reported in the literature [6, 11, 14, 25]. Although a higher carbonation conversion of coal fly ash (FA) can be achieved (i.e., 80–90%), the CaO content of coal fly ash is low (i.e., 5–10%), thereby resulting in a relatively low CO_2 capture capacity.

For determining CO_2 fixation capacity via the carbonation reaction, the available methods for the cases of mortars/concrete and cement kiln dust according to their physicochemical properties have been reported by Steinour [26] and Huntzinger et al. [27], which is as follows:

$$\begin{aligned} \mathrm{ThCO_2}(\%) = 0.785\,(&\mathrm{CaO} - 0.56\,\mathrm{CaCO_3} \\ &- 0.7\,\mathrm{SO_3}) + 1.091\,\mathrm{MgO} + 1.420\,\mathrm{Na_2O} + 0.935\,\mathrm{K_2O} \end{aligned} \tag{6.4}$$

Similarly, for the fresh alkaline solid waste, if it is assumed that all of the CaO content in the solid waste, except that originally bound in $CaSO_4$ and $CaCO_3$ phases, will convert to $CaCO_3$, the theoretical CO_2 capture capacity ($ThCO_2$, as a percentage of dry mass) can be estimated via Eq. (6.5):

$$\mathrm{ThCO_2}(\%) = 0.785\,(\mathrm{CaO} - 0.56\,\mathrm{CaCO_3} - 0.7\,\mathrm{SO_3}) \tag{6.5}$$

where $ThCO_2$ (kg CO_2/kg solid waste) is the theoretical CO_2 capture capacity, CaO (kg CaO/kg solid waste) and SO_3 (kg SO_3/kg solid waste) are the weight fraction of CaO and SO_3 in solid waste measured by XRF, respectively, and $CaCO_3$ (kg $CaCO_3$/kg solid waste) is the weight fraction of $CaCO_3$ analyzed by TGA.

Based on Eq. (6.5), the theoretical amount of CO_2 capture for different solid wastes is fall in the following ranges:

- Blast furnace slag (BFS): 0.252 − 0.322 kg-CO_2/kg-BFS,
- Basic oxygen furnace slag (BOFS): 0.309 − 0.374 kg-CO_2/kg-BOFS,
- Electric arc furnace oxidizing slag (EAFOS): 0.177 − 0.229 kg-CO_2/kg-EAFOS,
- Electric arc furnace reducing slag (EAFRS): 0.313 − 0.391 kg-CO_2/kg-EAFRS,
- Argon oxygen decarburization slag (AODS): 0.428 − 0.476 kg-CO_2/kg-AODS,
- Ladle furnace slag (LFS): 0.396 − 0.451 kg-CO_2/kg-LFS,
- Coal fly ash (FA): ~ 0.070 kg-CO_2/kg-FA,
- MSWI fly ash (FA): 0.323 − 0.388 kg-CO_2/kg-FA, and
- MSWI bottom ash (BA): 0.124 − 0.158 kg-CO_2/kg-BA.

In some cases, the probability of $MgCO_3$ formation is low due to the relatively low content of MgO in alkaline solid waste. Also due to the relatively low pressure of CO_2 and the short reaction time, limited $MgCO_3$ formation is expected. Typical process conditions for the formation of $MgCO_3$ via aqueous carbonation are (1) p_{CO_2} greater than 100 bar, (2) temperature greater than 144 °C, and (3) a reaction time of hours [28, 29]. The other metal oxide components, such as SiO_2 and P_2O_5, in the fresh solid waste are considered not to contribute to CO_2 fixation.

6.1.4 Kinetics and Thermodynamics of Thermal Decomposition

The kinetic (i.e., apparent activation energy, kinetic exponent, and pre-exponential factor) and thermodynamic parameters (i.e., the changes of entropy, enthalpy, and Gibbs free energy for the formation of the activated complex) for the thermal decomposition of a certain compound in a material can be determined by the Kissinger equation and Arrhenius equation, and transition state theory.

6.1.4.1 Kinetic Equations

The Kissinger equation has been extensively applied to evaluate the kinetics of thermal decomposition of a solid material, and the relevant activation energy and reaction order [30–34]. First, the reaction rate of a solid-state reaction can be expressed by means of the general mass action law with the Arrhenius law, as shown in Eq. (6.6):

$$\frac{d\alpha}{dt} = k(T)f(\alpha) = A\exp\left(-\frac{E_a}{RT}\right)f(\alpha) \tag{6.6}$$

where k is the rate constant, T is the absolute temperature (K), α(-) is the reacted fraction, $f(\alpha)$ is an algebraic function depending on the reaction mechanism, A is the pre-exponential factor (1/min), E_a is the apparent activation energy (kJ/mol), and R is the universal gas constant (8.314 J/K mol).

Then, by differentiating Eq. (6.6), if the temperature (T) rises at a constant heating rate (β = dT/dt), Eq. (6.7) can be obtained for a non-isothermal kinetics [34]:

$$\frac{d^2\alpha}{dt^2} = \left[\beta\frac{E_a}{RT^2} + A\exp\left(-\frac{E_d}{RT}\right)f'(\alpha)\right]\frac{d\alpha}{dt} \tag{6.7}$$

where β is the heating rate (K/min), and T_p is the absolute temperature of peak (K).

After that, assuming the maximum rate occurs at a temperature T_p, i.e., $\left[d(d\alpha/dt)_{T_p}/dt\right] = 0$, the general form of Kissinger equation for a non-isothermal kinetics can be expressed as Eq. (6.8), for the determination of the activation energy.

$$\ln\left(\frac{\beta}{T_p^2}\right) = -\frac{E_a}{R}\frac{1}{T_p} + \ln\left(-\frac{ARf'(\alpha)}{E_a}\right) = C_1\frac{1}{T_p} + C_2 \tag{6.8}$$

According to Eq. (6.8), the slope of the plot of ln (β/T_p^2) versus $1/T$ gives the apparent activation energy (E_a). The constant term (C_2), i.e., the intercept with the *y*-axis, is related to both A and $f'(\alpha)$, as shown in Eq. (6.9):

$$C_2 = \ln\left(\frac{ARf'(\alpha)}{E_a}\right) \tag{6.9}$$

Also, we can assume the temperature independence of the pre-exponential factor based on the Arrhenius theory. The rate of a thermally induced solid reaction can be expressed as Eq. (6.10):

$$\frac{d\alpha}{dT} = \frac{Af(\alpha)}{\beta}\exp\left(-\frac{E_a}{RT_p}\right) \tag{6.10}$$

As applied frequently for a description of heterogeneous processes with the surface reaction controlled [31], the $f(\alpha)$ can be expressed by the reaction order kinetic model:

$$f(\alpha) = (1-\alpha)^n \tag{6.11}$$

where n is the kinetic exponent of thermal decomposition reaction. By substitution of n from Eqs. (6.9) and (6.11) into Eq. (6.10) and rearranging, the value of the kinetic exponent (n) can be estimated directly from Eq. (6.12):

$$n = \frac{(1-\alpha_{max})}{d\alpha_{max}/dT}\frac{E_a}{\beta R}\exp(C_2)\exp\left(-E_a/RT_p\right) \tag{6.12}$$

Furthermore, according to Kissinger [35], the n value for reaction order processes can be estimated by the shape index (SI) if the peak shape is independent of heating rate (Eq. 6.13). The SI value of the DTG curve is an important parameter of thermodynamic analysis. The definition of SI value can refer to Fig. 6.4.

$$n = 1.26\,\mathrm{SI}^{1/2} \tag{6.13}$$

Carne et al. [36] also proposed possibilities to evaluate the n value from the slope of the plot of ln β versus $1/T_p$ as in Eq. (6.14):

$$\frac{d\,ln\beta}{d(1/T_p)} = -\frac{E_a}{nR} \tag{6.14}$$

6.1.4.2 Thermodynamic Equations

For decomposition thermodynamics of a certain compound in alkaline solid wastes, the transition state theory (so-called activated complex theory) can be applied. It can be described by the general form of the Eyring equation [30] in Eq. (6.15):

$$A = \frac{e \cdot \chi \cdot k_B \cdot T_p}{h} \exp\left(\frac{\Delta S}{R}\right) \tag{6.15}$$

where e is the Neper number (i.e., 2.7183), χ is the transition factor (i.e., 1 for monomolecular reactions), k_B is the Boltzmann constant (i.e., 1.381×10^{-23} J K^{-1}), and h is the Plank constant (i.e., 6.626×10^{-34} J s). The change of entropy (ΔS) term can be calculated based on the peak temperature (T_p) which characterizes the highest rate for thermal decomposition in the DTG plot. Therefore, the ΔS can be determined by rearranging Eq. (6.15), which is as follows:

$$\Delta S = R \ln\left(\frac{Ah}{e\chi k_B T_p}\right) \tag{6.16}$$

For the activated complex formation, the changes of the enthalpy (ΔH) and Gibbs free energy (ΔG) can be calculated using Eqs. (6.17) and (6.18), respectively:

$$\Delta H = E_a - RT_p \tag{6.17}$$

$$\Delta G = \Delta H^{\neq} - T_p \Delta S \tag{6.18}$$

6.1.5 Case Study: Basic Oxygen Furnace Slag

6.1.5.1 Modified TG-DTG Interpretation

Figure 6.6a, b shows the TG-DTG plots of the fresh and carbonated basic oxygen furnace slag (BOFS), respectively. The results show a continuous weight loss at 200–900 °C in both the fresh and carbonated BOFS, which is attributed to the decomposition of various hydrates, such as α-dicalcium silicate hydrate. Therefore, the thermal decomposition of various hydrates should be considered when determining the carbonate contents in BOFS. Other major minerals in BOFS, including brownmillerite, wollastonite, and larnite, are relatively stable compounds under the temperature range of TG analysis. In the fresh BOFS, the thermal decomposition of portlandite ($Ca(OH)_2$) occurs at temperature 400–500 °C. However, after carbonation, there was a lack of a peak for $Ca(OH)_2$ decomposition in BOFS, indicating

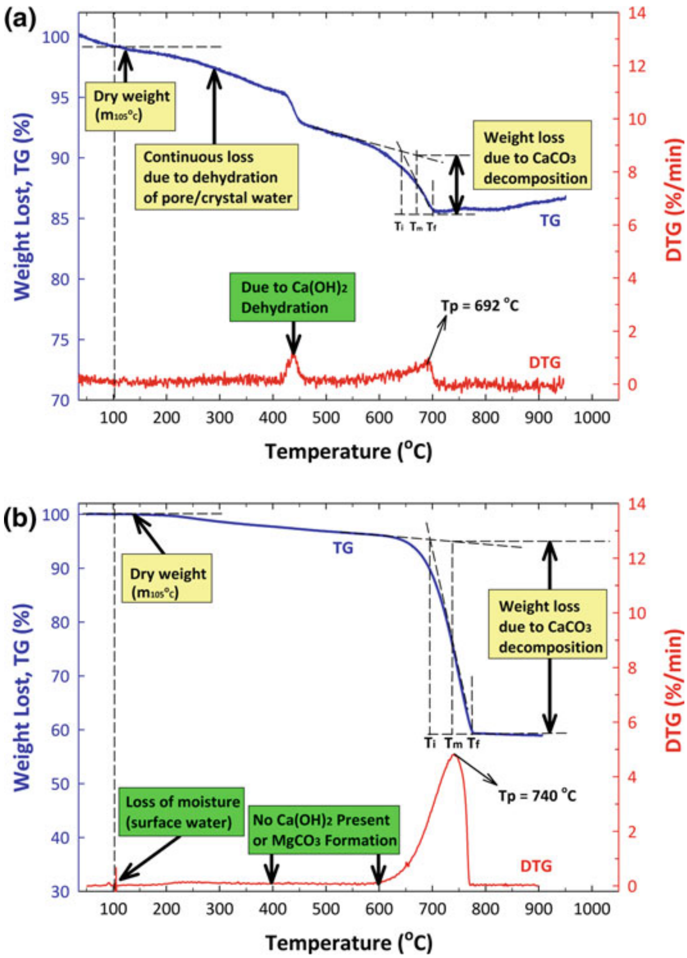

Fig. 6.6 TG-DTG plots for **a** fresh and **b** carbonated BOFS using the modified TG-DTG interpretation. Adaptation with permission from Macmillan Publishers Ltd: ref. [24], copyright 2016

that the $Ca(OH)_2$ was reacted with CO_2 during carbonation. Instead, a great weight loss at 600–800 °C was found in the carbonated BOFS, revealing the formation of $CaCO_3$ after carbonation.

On the other hand, no $MgCO_3$ formation was observed in the carbonated BOFS due to no peak at 500–630 °C in DTG, which was in good agreement with the XRD results [37, 38]. As the aforementioned, the typical conditions for the formation of $MgCO_3$ precipitates by aqueous carbonation are at a temperature over 144 °C [28] for hours [39]. Under the mild condition, with a ratio of Mg^{2+} to Ca^{2+} concentrations higher than 0.5, a metastable (amorphous) hydrated magnesium carbonate phase might be formed [23]. However, since the leaching concentrations of Mg ions from BOFS were low (e.g., 1.7–3.0 mg/L) [40], the formation of $MgCO_3$ crystal is negligible. In other words, the calcium-containing compositions in BOFS should be the major species reacting with CO_2 to form $CaCO_3$ precipitate.

To confirm the $CaCO_3$ content in BOFS, the DSC technique can be coupled with the TG analysis. The DSC technique can provide quantitative measurement on the heat released or absorbed by the specimen during heating. Theoretically, the $CaCO_3$ crystal will start to decompose into $CaO_{(s)}$ and $CO_{2(g)}$ at temperatures above 600 °C, as shown in Eq. (6.19). It is noted that the reaction heat for decomposing one mole of $CaCO_3$ particles at 1000 K is about 170.4 kJ [41]. Since the amounts of heat absorbed can be converted into the weight of $CaCO_3$ decomposed, the correlation between DSC and TG measurements can be established.

$$CaCO_{3(s)} \underset{\Delta}{\longrightarrow} CaO_{(s)} + CO_{2(g)}, \quad \Delta H^{o}_{1000\,K} = 170.4\,kJ/mol \tag{6.19}$$

Figure 6.7 shows the correlation between the amounts of $CaCO_3$ decomposition from modified TG-DTG interpretation (i.e., abscissa) and the heat absorbed from DSC technique (i.e., ordinate). The values of relative percent difference between the weights of $CaCO_3$ determined by thermography and those calculated from DSC are 1.34 ± 0.20%. Moreover, the results of paired-samples *t* tests indicated that the calculated *t*-value of 1.595 was less than the tabulated *t*-value of 2.201, thereby accepting the null hypothesis. In other words, no difference was found in $CaCO_3$ contents calculated from the modified TG-DTG interpretation and DSC method

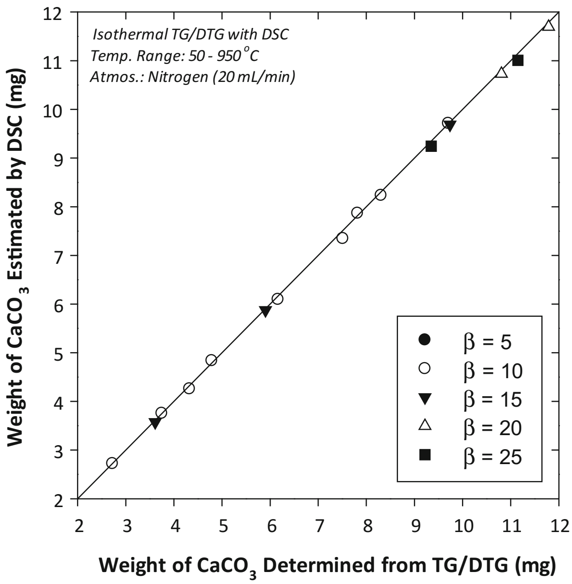

Fig. 6.7 Correlation of TG-DTG and DSC results for reference pure $CaCO_3$ powder under thermal decomposition. Adaptation with permission from Macmillan Publishers Ltd: ref. [24], copyright 2016

(p = 0.139), with a Pearson's correlation coefficient of 0.9997. This suggests that the modified TG-DTG interpretation should be applicable to provide a precise and accurate analysis of $CaCO_3$ contents in BOFS.

6.1.5.2 Qualitative Analysis by TG-MS

The weight loss between 500 and 900 °C would be simultaneously attributed to the decomposition of carbonates (release CO_2) and hydrates (release H_2O). To identify the types of volatiles and/or gases released during TG analysis, MS and/or FTIR can be used for the evolved gas analysis. For instance, Fig. 6.8a, b show the

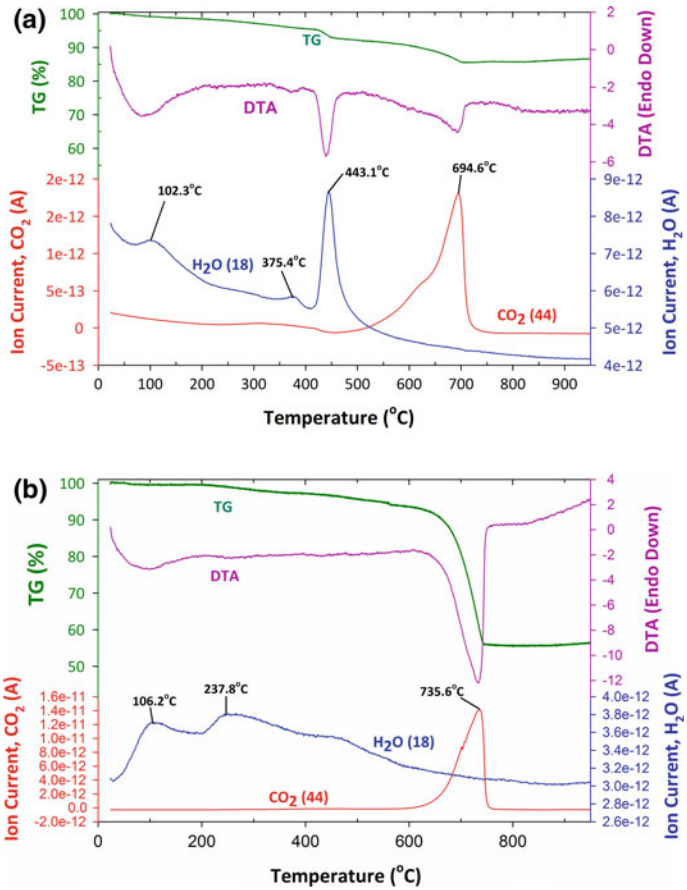

Fig. 6.8 Plots of weight loss (TG Analysis) and mass spectroscopy (ion current for H_2O mass number 18 and CO_2 mass number 44) for **a** fresh and **b** carbonated steel slag. Adaptation with permission from Macmillan Publishers Ltd: ref. [24], copyright 2016

TG-MS plots of both fresh and carbonated BOFS, respectively. The dehydration of different hydrates was found to occur continuously between 50 and 800 °C, especially pronounced before 700 °C. The dissociation of the phases containing H_2O in fresh BOFS consists of three peaks at 102, 375, and 443 °C, which could be attributed to (1) evaporation of surface water, (2) evaporation of pore water, and (3) dehydration of crystal water (i.e., $Ca(OH)_2$), respectively. Similarly, two peaks for the H_2O signal in the carbonated BOFS were observed at 106 and 238 °C, revealing subsequent removal of surface water and pore water, respectively. The $Ca(OH)_2$ content was eliminated after carbonation because no H_2O signal was observed at 400–500 °C. It suggests that the series of H_2O signals in the evolved gas analysis results provides the evidence to the observations in TG-DTG plot.

In addition, in fresh BOFS, CO_2 evolved gas coming from the decomposition of $CaCO_3$ was observed at 695 °C. Similar results were observed in the carbonated BOFS that the loss of mass occurring at 650–750 °C is related to CO_2 emissions, corresponding to the decomposition of $CaCO_3$, with a high temperature peak of 736 °C. This confirmed that the carbonate product is a crystallized $CaCO_3$. Furthermore, no peak of the CO_2 signal was observed at 500–600 °C after carbonation, revealing that the decomposition of $MgCO_3$ crystal was not detected. This provided the rationale that the formation of $MgCO_3$ was negligible in the case of BOFS.

6.1.5.3 Thermal Decomposition Kinetics and Thermodynamics

To determine the kinetic parameters for the thermal decomposition of $CaCO_3$ in BOFS, Table 6.2 presents the influence of heating rate (β) on important peak parameters, including T_i, T_e, W, $W_{1/2}$, H, and SI value. The results indicate that the peak temperature of $CaCO_3$ decomposition (T_p) increases with the increase of the heating rate [24].

Figure 6.9 illustrates the value of E_a estimated from the slope of the Kissinger plot, indicating that the E_a yields 197.7 ± 5.5 kJ/mol with an R^2 value of 0.995. Typically, the activation energy increases as the particle size increases [22, 42]. The E_a values for the cases of pure $CaCO_3$ powder [2, 32, 33, 42] and $CaCO_3$ mixture [22, 30, 43] were in the ranges of 139.0–190.4 and 119.7–179.4 kJ/mol, respectively. In this case study, the obtained E_a value (i.e., 198 kJ/mol) is higher than the value of theoretical E_a for thermal decomposition of isolated calcite $CaCO_3$ (i.e., 175 kJ/mol) [43]. This might be attributed to the fact that calcite was formed inside BOFS particles and/or on the surface of BOFS particles, which required extra energy to overcome the barrier of an impure layer.

As presented in Table 6.3, the reaction order (n) value can be determined by several approaches, including the reaction order model, the SI of peak, and the

Table 6.2 Effect of heating rate (β) on the peak parameters of DTG curve under N_2 atmosphere. Reprinted by permission from Macmillan Publishers Ltd: ref. [24], copyright 2016

β ($K\ min^{-1}$)	T_i (K)	T_p (K)	T_f (K)	W (K)	$W_{1/2}$ (K)	H (% K^{-1})	T_2/T_1 ratio	SI
1	869.0 ± 1.1	947.4 ± 3.7	958.6 ± 3.2	89.6 ± 2.1	51.8 ± 1.7	0.64 ± 0.01	1.08 ± 0.00	0.14 ± 0.02
5	906.3 ± 3.4	1011.4 ± 4.3	1035.9 ± 5.5	124.1 ± 4.1	70.1 ± 2.2	2.50 ± 0.06	1.09 ± 0.01	0.19 ± 0.02
10	931.3 ± 5.1	1034.0 ± 4.2	1060.3 ± 8.3	129.0 ± 3.2	75.6 ± 4.3	4.45 ± 0.13	1.10 ± 0.01	0.26 ± 0.04
15	943.5 ± 1.8	1048.9 ± 5.7	1079.5 ± 7.3	136.0 ± 5.6	82.5 ± 2.1	6.40 ± 0.23	1.10 ± 0.02	0.26 ± 0.01
20	952.8 ± 0.9	1061.8 ± 2.4	1095.4 ± 0.8	142.5 ± 1.1	85.8 ± 1.5	8.26 ± 0.07	1.10 ± 0.01	0.30 ± 0.01
25	958.3 ± 0.7	1077.7 ± 3.0	1123.0 ± 1.6	164.8 ± 1.4	99.0 ± 2.0	8.86 ± 0.12	1.12 ± 0.00	0.33 ± 0.05
30	963.8 ± 3.0	1087.0 ± 5.2	1136.7 ± 8.5	172.9 ± 7.8	105.3 ± 5.1	10.1 ± 0.4	1.12 ± 0.01	0.39 ± 0.06
35	965.9 ± 0.8	1087.9 ± 3.5	1137.9 ± 6.8	172.0 ± 6.6	103.7 ± 3.0	12.0 ± 0.4	1.12 ± 0.01	0.41 ± 0.01

Note All experiments were carried out with triple duplicates ($N = 3$)

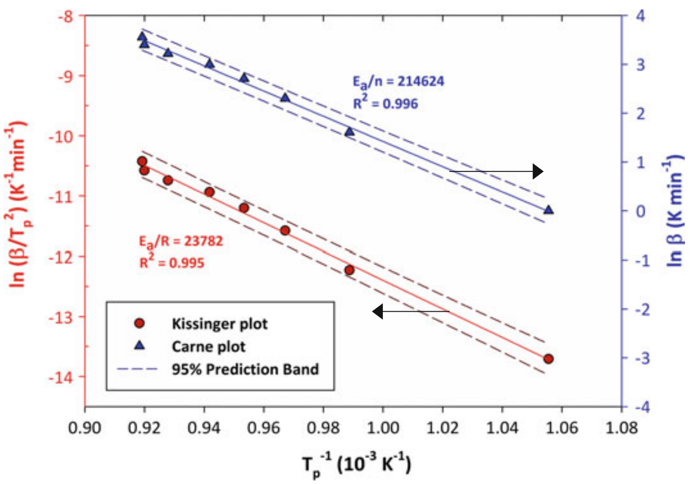

Fig. 6.9 Evaluation of apparent activation energy (via Kissinger plot) and reaction order (via Carne plot) of $CaCO_3$ thermal decomposition in steel slag. Adaptation with permission from Macmillan Publishers Ltd: ref. [24], copyright 2016

Carne equation. The *n* values determined from the reaction order model and the SI of peaks are 0.11–2.58 and 0.47–0.81, respectively. This indicates that the *n* value is sensitive to heating conditions. The methods applied for calculation of the *n* value provide considerably different results. Based on the Carne plot, the *n* value is estimated to be 0.92 ± 0.03, with the highest R^2 value of 0.996 among the three applied methods. As a result, the $CaCO_3$ decomposition in BOFS can be considered as a first-order reaction, implying interface-controlled growth with grain boundary nucleation after saturation [44]. Similar results ($n \cong 1$) were also observed in the literature [22, 30, 32, 33, 42, 43]. To determine the pre-exponential factor (*A*), the *n* value from the Carne method can be used. Substitution of E_a and *n* values into Eq. (6.7) provides an average value of *A* of $(2.20 \pm 0.01) \times 10^9$ min^{-1}. It is noted that the *A* value regularly increased with the heating rate.

On the other hand, the thermodynamic parameters, including ΔS, ΔH, and ΔG, can be determined using general equations. As presented in Table 6.3, the average value of ΔS was estimated to be about −118.82 J/mol K. This indicated that the formation of the activated complex exhibited a more organized structure than the initial substance. In addition, the average values of ΔH and ΔG were 189.04 and 313.16 kJ/mol, respectively [24]. For $CaCO_3$ decomposition, the ΔH values are close to the E_a values. However, significant differences between the values of ΔH and ΔS are observed.

Table 6.3 Kinetic and thermodynamic parameters determined by Kissinger calculation procedure. Adaptation with permission from Macmillan Publishers Ltd: ref. [24], copyright 2016

β (K/min)	$\times 10^{-3}$ 1/T_p (1/K)	$(1 - \alpha_{max})^a$	$\times 10^{-2}$ $d\alpha_{max}/dT$ (1/K)^a	n value			A ($\times 10^9$ 1/min)^b	ΔS (J/mol K)	ΔH (kJ/mol)	ΔG (kJ/mol)
				Kissinger (Eq. 6.12)	Kissinger (Eq. 6.13)	Carne (Eq. 6.14)				
1	1.0555	0.646 ± 0.008	0.657 ± 0.005	2.58	0.47	0.92	2.194	−118.05	189.84	301.69
5	0.9887	0.676 ± 0.018	2.542 ± 0.065	0.68	0.55	0.92	2.202	−118.57	189.31	309.23
10	0.9671	0.671 ± 0.007	4.572 ± 0.115	0.31	0.64	0.92	2.201	−118.75	189.12	311.91
15	0.9534	0.694 ± 0.002	6.507 ± 0.250	0.21	0.65	0.92	2.207	−118.85	189.00	313.66
20	0.9418	0.693 ± 0.004	8.401 ± 0.069	0.16	0.69	0.92	2.207	−118.95	188.89	315.20
25	0.9279	0.694 ± 0.005	9.081 ± 0.131	0.17	0.73	0.92	2.207	−119.08	188.76	317.09
30	0.9199	0.701 ± 0.005	10.35 ± 0.38	0.15	0.79	0.92	2.209	−119.14	188.68	318.19
35	0.9192	0.702 ± 0.007	12.28 ± 0.34	0.11	0.81	0.92	2.209	−119.15	188.67	318.29

[a] Data with 95% confidence interval
[b] The pre-exponential factor was determined by Eqs. (6.7) and (6.14) (n = 0.92)

6.2 Quantitative X-ray Diffraction (QXRD)

Considerable research has been carried out on solid wastes and/or industrial by-products in various domains: accelerated carbonation [37, 45], utilization performance [46, 47], and environmental impact [48, 49]. Although these research studies were performed for a variety of purposes, a common point is that the properties of the material should be characterized in advance. The characterization of a material is usually divided into three parts:

- Physical properties: morphology, fitness, density, solubility, etc.
- Chemical properties: oxide contents, heavy metal leaching amounts, hazardous components, pozzolanic and cementitious properties, etc.
- Mineralogical properties: crystalline, phase fraction, grain size, defect, etc.

The physical properties would greatly influence their reactivity with the environment. The chemical properties would give a first direction of the wastes' hazard potential. The mineralogical analysis of the wastes would provide further understanding on their behavior according to their nature and proportion of various mineral phases. The quantitative mineralogical characterization of waste is an essential step. Nevertheless, accurate analysis of the content of calcium carbonate in alkaline solid wastes is a difficult task due to their complex composition.

The X-ray quantitative phase analysis method can be applied to analyze the content of calcium carbonate in BOFS before and after carbonation. Two types of analytical techniques using X-ray diffraction, such as reference intensity ratio method and Rietveld refinement, can provide precise and accurate information on the fraction of crystal phases in solid wastes, although they are generally time-consuming in sample preparation and data processing.

6.2.1 Reference Intensity Ratio (RIR)

Reference Intensity Ratio (RIR) method, based on the measurement of the diffraction intensities (areas) of the characteristic peaks of the minerals, has been used to quantify the mineral phase in solids, e.g., quartz [50] and carbonates [23]. Three samples are needed: (1) the raw material, (2) the pure mineral, and (3) a mixture containing a known mass of pure mineral per gram of raw material. The amount of the certain phase can be calculated as follows [50]:

$$x = a \cdot \frac{I}{I_0} \cdot \frac{I_0 - I'}{I' - I} \quad (6.20)$$

where x is the amount of the certain phase (in g/g of sample), and I, I_0, and I' are the intensities of the characteristic peak of the certain phase in the raw material, in the pure phase, and in the mixture containing a grams of the certain phase per gram of raw material, respectively. The RIR method can be also performed through the use of an internal standard, such as high-purity corundum α-Al_2O_3 crystal powder (>99.5%) [23].

6.2.2 *Rietveld Refinement*

Rietveld method has been considered a powerful tool for crystal structure refinements and quantitatively analysis [51] based on X-raydiffraction pattern. The Rietveld method considers overlapping peaks in the XRD pattern and the effect of preferred orientation [52]. Therefore, this method has been widely used on various materials, of which the mineralogy is well known, for instance, Portland cement [52]. Moreover, it has been applied for the quantification of various mineral crystals in solid wastes [50, 53–55].

Unlike chemical methods and thermal analysis, the Rietveld method does not change the state of samples and avoids side reactions in ambient conditions [52]. Additional advantages of using the Rietveld method for phase quantification included

- Time-consuming calibration measurements can be avoided.
- The phase abundance could be determined if all phases are identified and these crystal structure parameters and chemical composition are known.
- The relative weight fractions of crystalline phases in a multiphase sample could be calculated directly from scale factors of the respective calculated intensities.

Figure 6.10 illustrates the standard operation procedure of QXRD using Rietveld method for quantifying phase fraction in a material:

- Step 1: acquisition of XRD pattern of a material,
- Step 2: identification of the major crystal phases for the XRD pattern, and
- Step 3: application of Rietveld refinement technique to quantify the phase fraction and evaluate the crystal structure.

Fig. 6.10 QXRD procedure using Rietveld method for quantifying phase fraction in a material

6.2.2.1 Principles

Several factors, which may be responsible for the discrepancy of the quantitative results, can be obtained from the Rietveld method [51]:

- Sample preparation: It is impossible to get correct results in the case of an inhomogeneous sample.
- Structure model: Large *R* values occur when incorrect structure input or unknown phase presents.
- Data collection tragedy: Both the step size and scanning speed can cause error in the determination of X-ray diffraction peak positions, intensity, and full width at half maximum (FWHM). Intensity error caused by counting statistic will rise with increasing scanning rate and decreasing count time.

The Rietveld method is a full-pattern analysis that the atom parameters in the unit cell are calculated fitting the entire pattern by the least-squares method so that minimizing the difference (M) between the experimental ($y_{(\mathrm{obs})}$) and calculated ($y_{(\mathrm{calc})}$) XRD diffractogram [51, 56]:

$$M = \sum_{i=1}^{n} w_i \left[y_{i(\mathrm{obs})} - y_{i(\mathrm{calc})} \right]^2 = \text{minimum} \tag{6.21}$$

where w_i is the weight of each observation point, and n is the number of observation points. The sum i is over all data points. Therefore, the missing major phases in the Rietveld method would inevitably involve significant differences between experimental and calculated patterns.

The standard uncertainty of $Y_{O,i}$ (i.e., $\sigma[Y_{O,i}]$) can be determined by measuring the $Y_{O,i}$ intensity for an infinite number of times. To evaluate the goodness of the developed model, a statistical method such as chi-squared (χ^2) test should be introduced as follows:

$$\chi^2 = \frac{1}{n} \sum_{i=1}^{n} \frac{\left[Y_{O,i} - Y_{C,i} \right]^2}{\sigma^2[Y_{O,i}]} \tag{6.22}$$

Typically, the χ^2 value would gradually converge to one during the Rietveld refinement. By adjusting the key structure parameters, including background coefficients, cell parameters, zero-shifting error, peak shape parameters, and phase fractions, the difference between actual and simulated XRD patterns can be minimized. If the crystallographic model is correct and chemically reasonable, the χ^2 would never drop below or equivalent to one [57]. Also, the reliability of the refinement result should be judged by the goodness of fit (GOF), as determined by Eq. (6.23):

$$\text{GOF} = R_{wp}/R_{exp} \tag{6.23}$$

where R_p and R_{wp} are the pattern R factor and the weighted pattern R factor, respectively.

6.2.2.2 Available Software for Pattern/Structure Refinement

The refinement of XRD patterns using Rietveld method can be executed by many efficient programs such as GSAS [53, 54], FULLPROF 2000 [52], SIROQUANT [23, 53, 58, 59], X'Pert HighScore Plus [60], DBWS9411 [51], and Maud [50]. In the Rietveld refinement, various corrections can be introduced, such as texture, absorption contrast, sample transparency, displacement, and microabsorption effect.

For instance, the Rietveld method can be performed by the General Crystal Structure Analysis System (GSAS) software with the EXPGUI program. GSAS was created by Larson and Von Dreele [61] of Los Alamos National Laboratory for fitting atomic structural models to single crystal and powder diffraction data, even both simultaneously. In GSAS, the atom parameters including scale factors, background coefficients, zero-shifting error, lattice parameters, profile shape parameters, atomic site occupancies, and phase fractions in the unit cell were refined simultaneously.

The crystal structure parameters used to interpret the XRD patterns can be taken from the ICSD (Inorganic Crystal Structure Database). Typically, the major components in alkaline solid wastes, with the collection codes for each structure, include

- α-dicalcium silicate hydrate ($Ca_2(HSiO_4)(OH)$, abbreviated as C_2–S–H, Code 75277),
- β-larnite (Ca_2SiO_4, abbreviated as C_2S, Code 245080),
- brownmillerite ($Ca_2Fe_{1.014}Al_{0.986}O_5$, Code 98836),
- calcite ($CaCO_3$, Code 169933),
- portlandite ($Ca(OH)_2$, Code 73468),
- wollastonite ($CaSiO_3$, abbreviated as C_1S, Code 240469), and
- wustite (FeO, Code 633038).

6.2.3 Case Study: Alkaline Solid Wastes

The Rietveld refinement has been considered to be chemically plausible by viewing the observed and calculated patterns graphically. Kuusik et al. [62] suggested that the compositions of oil shale ash have shown a good correlation between the chemical and quantitative XRD analyses, where the latter can be used for preliminary and rapid analysis. Mahieux et al. [50] determined the mineral composition of

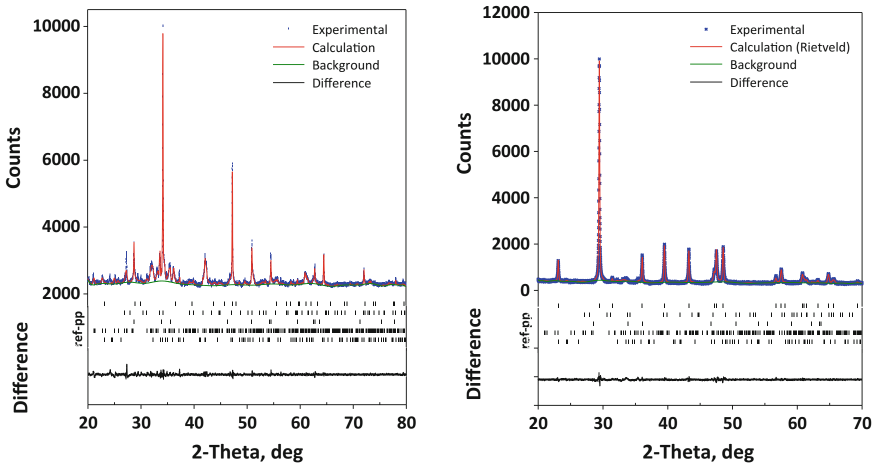

Fig. 6.11 Experimental and calculated XRD diffractogram by Rietveld method in GSAS program for (*left*) fresh and (*right*) carbonated BOFS. Reprinted with the permission from Ref. [40]. Copyright 2013 American Chemical Society

a sewage sludge ash and a municipal solid waste incineration fly ash by both physicochemical analysis and Rietveld method. The results obtained were coherent, suggesting that it is possible to quantify the mineral composition of complex mineral waste with Rietveld method.

For instance, in the case of basic oxygen furnace slag (BOFS), Fig. 6.11 shows the experimental and calculated diffractogram by the Rietveld method for the fresh and carbonated BOFS. The refinement results indicated that only a slight difference was observed in the intensity of major peaks between the experimental and calculated patterns by the Rietveld method. The obtained χ^2 values were 1.87 and 1.94 for fresh and carbonated BOFS, respectively, which was statistically acceptable [57]. Before carbonation, the principle components in BOFS were FeO (23%), $Ca_2Fe_{1.014}Al_{0.986}O_5$ (22%), $Ca(OH)_2$ (19%), C_2–S–H (15%), C_1S (11%), and $CaCO_3$ (10%). In the carbonated BOFS, the content of $CaCO_3$ increased significantly, while the contents of $Ca(OH)_2$, C_1S, C_2–S–H, and $Ca_2Fe_{1.04}Al_{0.986}O_5$ decreased [40]. Therefore, the mineral phases of $Ca(OH)_2$, C_1S, C_2–S–H, and $Ca_2Fe_{1.04}Al_{0.986}O_5$ in BOFS are regarded as the major species reacting with CO_2 to form $CaCO_3$ precipitation.

6.3 Scanning Electronic Microscopy

Scanning electron microscopy (SEM) equipped with X-ray energy-dispersive spectrometer (XEDS) is a useful tool for observing the surface structure of the sample and the elemental analysis of the solid surface. The SEM/XEDS technique involves analysis of thousands of pixels in a short time. The XEDS can record quantum energies between 1 and 40 keV, or higher, simultaneously by means of a multichannel analyzer [63]. Typically, the specimen before and after carbonation is mounted with double-sided carbon tape on an aluminum stub. For better conductivity and reduction of electron charge, the sample is usually coated with a thin layer of platinum.

6.3.1 Types of Techniques in SEM

6.3.1.1 Focused Ion Beam (FIB)

Focused ion beam (FIB) is a technique used in the SEM, where a FIB uses a focused beam of ions to image samples in the chamber, while the SEM uses a focused beam of electrons instead. Most widespread sources of ion beam are liquid metal ion source (LMIS), especially gallium (Ga) ion sources. The melting point of Ga metal is about 30 °C. In a Ga LMIS, gallium metal is placed in contact with a tungsten needle, where the radius of needle tip is typically $\sim$2 nm. The electric field at this tip is greater than 1×10^8 V/cm, causing ionization and field emission of the Ga atoms. Then, source ions are accelerated to an energy between 1 and 50 keV. Unlike an SEM, FIB is inherently destructive to the specimen since the high-energy Ga ions will sputter atoms from the surface. Therefore, the FIB can be used as a micro- and nanomachining tool to modify materials at the micro- and nanoscale.

6.3.1.2 Mapping

Elemental mapping technique uses X-ray counts from thousands of points on a particle surface. The data is collected in less than 1 h and analyzed to provide frequency distribution curves and relative elemental abundance [63]. In general, mapping of Ca, Mg, Fe, Si, C, and O is carried out for alkaline solid wastes to evaluate the distribution of these elements on the sample particles.

6.3.1.3 Cross-Sectional Images

Superficial and cross-sectional observations can be performed on the specimens. For cross-sectional analyses, samples usually are cut and mounted with epoxy resin in a plastic holder. The surface also can be polished with SiC paper and/or alumina. Nital (i.e., a solution of alcohol and nitric acid) etching can be performed for a better characterization of the samples. Similarly, fine gold films can be sputtered on the, otherwise insulating, samples.

6.3.2 Case Study: Carbonation of Steel Slag

Figure 6.12 shows the cross-sectional images and elemental mapping of fresh steel slag. Before carbonation, the entire steel slag is rich in calcium–ferrous–silicate (Ca–Fe–Si oxide) and/or calcium–magnesium–silicate (Ca–Mg–Si oxide) but without carbon (C) element. The distribution of the chemical elements was observed to be inhomogeneous from particle to particle. Meanwhile, the distribution of the calcium is quite concentrated in both of the fresh and carbonated steel slag. Generally, the distribution percentage of the carbon on the surface of the carbonated steel slag is found to be higher than that on the fresh steel slag, which indicates that the CO_2 can be captured successfully by carbonation reaction.

Figure 6.13 shows the cross-sectional images and elemental mapping of carbonated steel slag. After carbonation, the steel slag exhibits rhombohedral crystals, with a size of 1–3 µm, formed uniformly on the surface of the slag, exhibiting an outside $CaCO_3$ product layer (reacted) and an inside metal-rich core (unreacted).

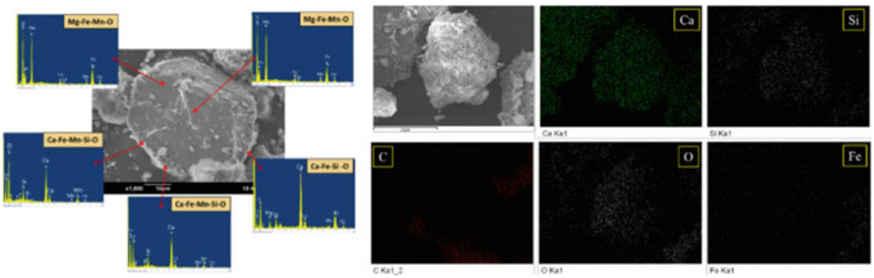

Fig. 6.12 (*Left*) cross-sectional observations and (*right*) elemental mapping of fresh steel slag by SEM/XEDS. Ca, Mg, Fe, Si, C, and O are recorded during the scanning of samples. Reprinted with the permission from ref. [40]. Copyright 2013 American Chemical Society

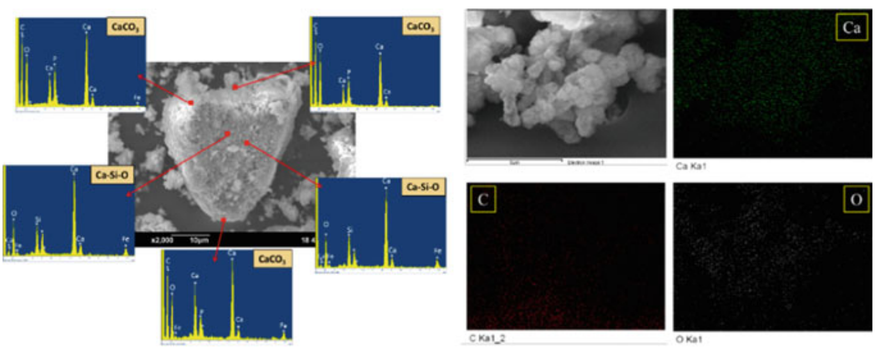

Fig. 6.13 (*Left*) Cross-sectional observations and (*right*) elemental mapping of carbonated steel slag by SEM/XEDS. Ca, Mg, Fe, Si, C, and O are recorded during the scanning of samples. Reprinted with the permission from Ref. [40]. Copyright 2013 American Chemical Society

Moreover, the cubic-shaped crystals coating the surface of carbonated steel slag are composed of calcium, carbon, and oxygen elements, indicating the formation of $CaCO_3$ (calcite). Similarly, the observations of SEM/XEDS and mappings are in good agreement with the results of QXRD using the Rietveld method [40].

References

1. Speyer RF (1994) Thermal analysis of materials. Marcel Dekker Inc., New York
2. Escardino A, García-Ten J, Feliu C, Saburit A, Cantavella V (2013) Kinetic study of the thermal decomposition process of calcite particles in air and CO_2 atmosphere. J Ind Eng Chem 19(3):886–897. doi:10.1016/j.jiec.2012.11.004
3. Villain G, Thiery M, Platret G (2007) Measurement methods of carbonation profiles in concrete: thermogravimetry, chemical analysis and gammadensimetry. Cem Concr Res 37 (8):1182–1192. doi:10.1016/j.cemconres.2007.04.015
4. Marsh BK, Day RL (1988) Pozzolanic and cementitious reactions of fly ash in blended cement pastes. Cem Concr Res 18:301–310
5. Tai CY, Chen WR, Shih S-M (2006) Factors affecting wollastonite carbonation under CO_2 supercritical conditions. AIChE J 52(1):292–299. doi:10.1002/aic.10572
6. Li W, Li B, Bai Z (2009) Electrolysis and heat pretreatment methods to promote CO_2 sequestration by mineral carbonation. Chem Eng Res Des 87(2):210–215. doi:10.1016/j.cherd.2008.08.001
7. Teir S, Eloneva S, Fogelholm C, Zevenhoven R (2009) Fixation of carbon dioxide by producing hydromagnesite from serpentinite. Appl Energy 86(2):214–218. doi:10.1016/j.apenergy.2008.03.013
8. Chang C, Chen J (2006) The experimental investigation of concrete carbonation depth. Cem Concr Res 36(9):1760–1767. doi:10.1016/j.cemconres.2004.07.025
9. Thiery M, Villain G, Dangla P, Platret G (2007) Investigation of the carbonation front shape on cementitious materials: effects of the chemical kinetics. Cem Concr Res 37(7):1047–1058. doi:10.1016/j.cemconres.2007.04.002
10. Bernal SA, de Gutierrez RM, Provis JL, Rose V (2010) Effect of silicate modulus and metakaolin incorporation on the carbonation of alkali silicate-activated slags. Cem Concr Res 40(6):898–907. doi:10.1016/j.cemconres.2010.02.003
11. Huijgen WJJ, Witkamp GJ, Comans RNJ (2005) Mineral CO_2 sequestration by steel slag carbonation. Environ Sci Technol 39(24):9676–9682
12. Santos RM, Van Bouwel J, Vandevelde E, Mertens G, Elsen J, Van Gerven T (2013) Accelerated mineral carbonation of stainless steel slags for CO_2 storage and waste valorization: effect of process parameters on geochemical properties. Int J Greenh Gas Control 17:32–45. doi:10.1016/j.ijggc.2013.04.004
13. Chang EE, Pan SY, Chen YH, Tan CS, Chiang PC (2012) Accelerated carbonation of steelmaking slags in a high-gravity rotating packed bed. J Hazard Mater 227–228:97–106. doi:10.1016/j.jhazmat.2012.05.021
14. Chen Y-T (2008) Effects of process variables on the conversion of BOF slag to carbonate. National Taiwan University, Taipei, Taiwan
15. Lekakh SN, Rawlins CH, Robertson DGC, Richards VL, Peaslee KD (2008) Kinetics of aqueous leaching and carbonization of steelmaking slag. Metall Mater Trans B 39(1): 125–134. doi:10.1007/s11663-007-9112-8
16. Chen Q, Zhang L, Ke Y, Hills C, Kang Y (2009) Influence of carbonation on the acid neutralization capacity of cements and cement-solidified/stabilized electroplating sludge. Chemosphere 74(6):758–764. doi:10.1016/j.chemosphere.2008.10.044

17. Huntzinger DN, Gierke JS, Kawatra SK, Eisele TC, Sutter LL (2009) Carbon dioxide sequestration in cement kiln dust through mineral carbonation. Environ Sci Technol 43(6): 1986–1992
18. Rendek E, Ducom G, Germain P (2006) Carbon dioxide sequestration in municipal solid waste incinerator (MSWI) bottom ash. J Hazard Mater 128(1):73–79. doi:10.1016/j.jhazmat.2005.07.033
19. Li X, Bertos MF, Hills CD, Carey PJ, Simon S (2007) Accelerated carbonation of municipal solid waste incineration fly ashes. Waste Manag 27(9):1200–1206. doi:10.1016/j.wasman.2006.06.011
20. Cappai G, Cara S, Muntoni A, Piredda M (2012) Application of accelerated carbonation on MSW combustion APC residues for metal immobilization and CO_2 sequestration. J Hazard Mater 207–208:159–164. doi:10.1016/j.jhazmat.2011.04.013
21. Baciocchi R, Costa G, Di Bartolomeo E, Polettini A, Pomi R (2009) The effects of accelerated carbonation on $CO(_2)$ uptake and metal release from incineration APC residues. Waste Manag 29(12):2994–3003. doi:10.1016/j.wasman.2009.07.012
22. Hohamed M, Yusup S, Maitra S (2012) Decomposition study of calcium carbonate in cockle shell. J Eng Sci Technol 7(1):1–10
23. Hosseini T, Selomulya C, Haque N, Zhang L (2015) Investigating the effect of the Mg^{2+}/Ca^{2+} molar ratio on the carbonate speciation during the mild mineral carbonation process at atmospheric pressure. Energy Fuel 29(11):7483–7496. doi:10.1021/acs.energyfuels.5b01609
24. Pan SY, Chang EE, Kim H, Chen YH, Chiang PC (2016) Validating carbonation parameters of alkaline solid wastes via integrated thermal analyses: principles and applications. J Hazard Mater 307:253–262. doi:10.1016/j.jhazmat.2015.12.065
25. Eloneva S, Teir S, Salminen J, Fogelholm CJ, Zevenhoven R (2008) Steel converter slag as a raw material for precipitation of pure calcium carbonate. Ind Eng Chem Res 47(18):7104–7111
26. Steinour HH (1959) Some effects of carbon dioxide on mortars and concrete—discussion. J Am Concr Inst 30:905–907
27. Huntzinger DN, Gierke JS, Sutter LL, Kawatra SK, Eisele TC (2009) Mineral carbonation for carbon sequestration in cement kiln dust from waste piles. J Hazard Mater 168(1):31–37. doi:10.1016/j.jhazmat.2009.01.122
28. Teir S (2008) Fixation of carbon dioxide by producing carbonates from minerals and steelmaking slags. Helsinki University of Technology
29. Huijgen WJJ, Comans RNJ (2006) Carbonation of steel slag for CO_2 sequestration: leaching of products and reaction mechanisms. Environ Sci Technol 40(8):2790–2796
30. Georgieva V, Vlaev L, Gyurova K (2013) Non-isothermal degradation kinetics of $CaCO_3$ from different origin. J Chem 2013:1–12. doi:10.1155/2013/872981
31. Ptáček P, Šoukal F, Opravil T, Havlica J, Brandštetr J (2011) The kinetic analysis of the thermal decomposition of kaolinite by DTG technique. Powder Technol 208(1):20–25. doi:10.1016/j.powtec.2010.11.035
32. Li X-G, Lv Y, Ma B-G, Wang W-Q, Jian S-W (2013) Decomposition kinetic characteristics of calcium carbonate containing organic acids by TGA. Arab J Chem. doi:10.1016/j.arabjc.2013.09.026
33. Halikia I, Zoumpoulakis L, Christodoulou E, Prattis D (2001) Kinetic study of the thermal decomposition of calcium carbonate by isothermal methods of analysis. Eur J Min Process Environ Prot 1(2):89–102
34. Chen D, Gao X, Dollimore D (1993) A generalized form of the Kissinger equation. Thermochim Acta 215:109–117
35. Kissinger HE (1957) Reaction kinetics in differential thermal analysis. Anal Chem 29(11): 1702–1706
36. Carne LW, Dynes PJ, Kaelble DH (1973) Analysis of curing kinetics in polymer composites. J Polym Sci Polym Lett Ed 11(8):533–540

37. Pan SY, Chen YH, Chen CD, Shen AL, Lin M, Chiang PC (2015) High-gravity carbonation process for enhancing CO_2 fixation and utilization exemplified by the steelmaking industry. Environ Sci Technol 49(20):12380–12387. doi:10.1021/acs.est.5b02210
38. Pan SY, Chiang PC, Chen YH, Tan CS, Chang EE (2013) Ex situ CO_2 capture by carbonation of steelmaking slag coupled with metalworking wastewater in a rotating packed bed. Environ Sci Technol 47(7):3308–3315. doi:10.1021/es304975y
39. Chang EE, Chiu A-C, Pan S-Y, Chen Y-H, Tan C-S, Chiang P-C (2013) Carbonation of basic oxygen furnace slag with metalworking wastewater in a slurry reactor. Int J Greenh Gas Control 12:382–389. doi:10.1016/j.ijggc.2012.11.026
40. Pan SY, Chiang PC, Chen YH, Chen CD, Lin HY, Chang EE (2013) Systematic approach to determination of maximum achievable capture capacity via leaching and carbonation processes for alkaline steelmaking wastes in a rotating packed bed. Environ Sci Technol 47 (23):13677–13685. doi:10.1021/es403323x
41. Tian S, Jiang J, Hosseini D, Kierzkowska AM, Imtiaz Q, Broda M, Mìller CR (2015) Development of a steel-slag-based, iron-functionalized sorbent for an autothermal carbon dioxide capture process. ChemSusChem 8:3839–3846. doi:10.1002/cssc.201501048
42. Criado JM, Ortega A (1992) A study of the influence of particle size on the thermal decomposition of $CaCO_3$ by means of constant rate thermal analysis. Thermochim Acta 195:163–167
43. Escardino A, García-Ten J, Feliu C, Moreno A (2010) Calcium carbonate thermal decomposition in white-body wall tile during firing. I. Kinetic study. J Eur Ceram Soc 30 (10):1989–2001. doi:10.1016/j.jeurceramsoc.2010.04.014
44. Málek J (1995) The applicability of Johnson-Mehl-Avrami model in the thermal analysis of the crystallization kinetics of glasses. Thermochim Acta 267:61–73
45. Santos RM, Chiang YW, Elsen J, Van Gerven T (2014) Distinguishing between carbonate and non-carbonate precipitates from the carbonation of calcium-containing organic acid leachates. Hydrometallurgy 147–148:90–94. doi:10.1016/j.hydromet.2014.05.001
46. Chen KW, Pan SY, Chen CT, Chen YH, Chiang PC (2016) High-gravity carbonation of basic oxygen furnace slag for CO_2 fixation and utilization in blended cement. J Clean Prod 124:350–360. doi:10.1016/j.jclepro.2016.02.072
47. Muhmood L, Vitta S, Venkateswaran D (2009) Cementitious and pozzolanic behavior of electric arc furnace steel slags. Cem Concr Res 39(2):102–109. doi:10.1016/j.cemconres.2008.11.002
48. Xiao L-S, Wang R, Chiang P-C, Pan S-Y, Guo Q-H, Chang EE (2014) Comparative life cycle assessment (LCA) of accelerated carbonation processes using steelmaking slag for CO_2 fixation. Aerosol Air Qual Res 14(3):892–904. doi:10.4209/aaqr.2013.04.012
49. Pan S-Y, Lorente Lafuente AM, Chiang P-C (2016) Engineering, environmental and economic performance evaluation of high-gravity carbonation process for carbon capture and utilization. Appl Energy 170:269–277. doi:10.1016/j.apenergy.2016.02.103
50. Mahieux PY, Aubert JE, Cyr M, Coutand M, Husson B (2010) Quantitative mineralogical composition of complex mineral wastes—contribution of the Rietveld method. Waste Manag 30(3):378–388. doi:10.1016/j.wasman.2009.10.023
51. Liu H, Kuo C (1996) Quantitative multiphase determination using the Rietveld method with high accuracy. Mater Lett 26:171–175
52. Zhou Y, Song W, Zeng X, Xie C (2012) Quantitative X-ray Rietveld analysis of metallic aluminum content in nano-aluminum powders. Mater Lett 67(1):177–179. doi:10.1016/j.matlet.2011.09.051
53. Dermatas D, Dadachov MS (2003) Rietveld quantification of montmorillonites in lead-contaminated soils. Appl Clay Sci 23(1–4):245–255. doi:10.1016/s0169-1317(03)00109-1
54. Fernández-Jiménez A, de la Torre AG, Palomo A, López-Olmo G, Alonso MM, Aranda MAG (2006) Quantitative determination of phases in the alkaline activation of fly ash. Part II: degree of reaction. Fuel 85(14–15):1960–1969. doi:10.1016/j.fuel.2006.04.006

55. Bodénan F, Deniard P (2003) Characterization of flue gas cleaning residues from European solid waste incinerators: assessment of various Ca-based sorbent processes. Chemosphere 51 (5):335–347. doi:10.1016/s0045-6535(02)00838-x
56. Rietveld HM (1969) A profile refinement method for nuclear and magnetic structures. J Appl Crystallogr 2:65–71
57. Toby BH (2012) R factors in Rietveld analysis: how good is good enough? Powder Diffr 21 (01):67–70. doi:10.1154/1.2179804
58. Liu Q, Maroto-Valer MM (2012) Studies of pH buffer systems to promote carbonate formation for CO_2 sequestration in brines. Fuel Process Technol 98:6–13. doi:10.1016/j.fuproc.2012.01.023
59. Uibu M, Kuusik R, Andreas L, Kirsimäe K (2011) The CO_2-binding by Ca-Mg-silicates in direct aqueous carbonation of oil shale ash and steel slag. Energy Procedia 4:925–932. doi:10.1016/j.egypro.2011.01.138
60. Saito T, Sakai E, Morioka M, Otsuki N (2010) Carbonation of r-Ca_2SiO_4 and the mechanism of vaterite formation. J Adv Concr Technol 8(3):273–280
61. Larson AC, Von Dreele RB (1986) Generalized crystal structure analysis system. LAUR 86–748
62. Kuusik R, Uibu M, Kirsimäe K (2005) Characterization of oil shale ashes formed at industrial-scale CFBC boilers. Oil Shale 22:407–420
63. Alsmadi BM, Fox P (2001) Semi-quantitative analysis of changes in soil coatings by scanning electron microscope and energy dispersive X-ray mapping. Colloids Surf A 194:249–261